Excitonic magneto-optics in monolayer transition metal dichalcogenides: From nanoribbons to two-dimensional response

J. Have,[1,2,*] N. M. R. Peres,[3,4] and T. G. Pedersen[1,5]

[1]*Department of Materials and Production, Aalborg University, DK-9220 Aalborg East, Denmark*
[2]*Department of Mathematical Sciences, Aalborg University, DK-9220 Aalborg East, Denmark*
[3]*International Iberian Nanotechnology Laboratory (INL), 4715-330 Braga, Portugal*
[4]*Center and Department of Physics, and QuantaLab, University of Minho, Campus de Gualtar, 4710-057 Braga, Portugal*
[5]*Center for Nanostructured Graphene (CNG), DK-9220 Aalborg East, Denmark*

(Received 20 May 2019; revised manuscript received 24 June 2019; published 15 July 2019)

The magneto-optical response of monolayer transition metal dichalcogenides, including excitonic effects, is studied using a nanoribbon geometry. We compute the diagonal optical conductivity and the Hall conductivity. Comparing the excitonic optical Hall conductivity to results obtained in the independent-particle approximation, we find an increase in the amplitude corresponding to one order of magnitude when excitonic effects are included. The Hall conductivities are used to calculate Faraday rotation spectra for MoS_2 and WSe_2. Finally, we have also calculated the diamagnetic shift of the exciton states of WSe_2 in different dielectric environments. Comparing the calculated diamagnetic shift to recent experimental measurements, we find a very good agreement between the two.

DOI: 10.1103/PhysRevB.100.045411

I. INTRODUCTION

With the successful exfoliation of monolayers of transition metal dichalcogenides (TMDs) [1], a new group of interesting semiconducting materials became available for study and potential applications. The characteristics of monolayer TMDs include a direct band gap [1–3], broken inversion symmetry [4,5], strong spin-orbit coupling [6], and strongly bound excitons and excitonic complexes [7–10]. In addition to these characteristics, monolayer TMDs have also been shown to exhibit interesting magneto-optical properties such as valley polarized Landau levels [11–13], valley Zeeman splitting [14–18], and magnetic-field-induced rotation of the polarization state of light [19,20]. These properties have inspired potential new applications in areas such as optoelectronics [21] and valleytronics [22,23]. Magnetic fields have also been used to probe exciton properties, such as effective mass, size [24–26], and how they are affected by the dielectric environment [27].

So far, the theoretical analysis of TMD magnetoexcitons has relied on effective-mass models, such as the Wannier model [10,24,27,28]. We recently validated that the Wannier model can be used to accurately describe certain properties of magnetoexcitons [29]. However, in the Wannier model, the Bloch part of the wave function is replaced by a plane wave, which makes the task of computing the single-particle momentum matrix elements unfeasible. For the diagonal optical response there is a solution to this problem [30], but for the Hall conductivity no solution currently exists. Thus, the Wannier model cannot be applied to the task of calculating the Hall conductivity, which is a necessary step in computing the magneto-optical Kerr effect and the Faraday rotation [31,32]. The issue can be resolved in the independent-particle approximation (IPA) [13,33,34], but the optical properties of TMDs are dominated by excitonic effects. Hence, for an accurate description of the magneto-optical response of TMDs, excitons should be included.

The main computational difficulty in going beyond effective mass models when treating magnetoexcitons is that the external magnetic field breaks the translation symmetry of the single-particle Hamiltonian. Depending on the choice of magnetic vector potential gauge, translation symmetry will be broken in at least one direction. The translation symmetry can be restored by considering a magnetic supercell, but the size of the supercell is inversely proportional to the magnetic field strength [33]. Consequently, for experimentally obtainable field strengths, a very large supercell is needed, thus making the task of computing the excitonic properties unfeasible [35]. In the present work, we address this issue by using a system of finite width in the direction, for which translation symmetry is broken. This approach corresponds to considering wide TMD nanoribbons. By increasing the size of the system in the finite direction, we are able to recover the two-dimensional (2D) response, including excitonic effects. Using this approach, we then describe quantitatively the excitonic effects on both the diagonal conductivity and the Hall conductivity of monolayer TMDs perturbed by an external magnetic field. This allows us to compute Faraday rotation spectra as well as excitonic diamagnetic shifts.

The paper is structured as follows: In Sec. II, the tight-binding model used to describe the single-particle properties of both 2D monolayer TMDs and nanoribbons is introduced. In this section, we also check the width convergence of the nanoribbon optical response in the independent-particle approximation. In Sec. III, we include excitonic effects in our

---

[*] jh@nano.aau.dk

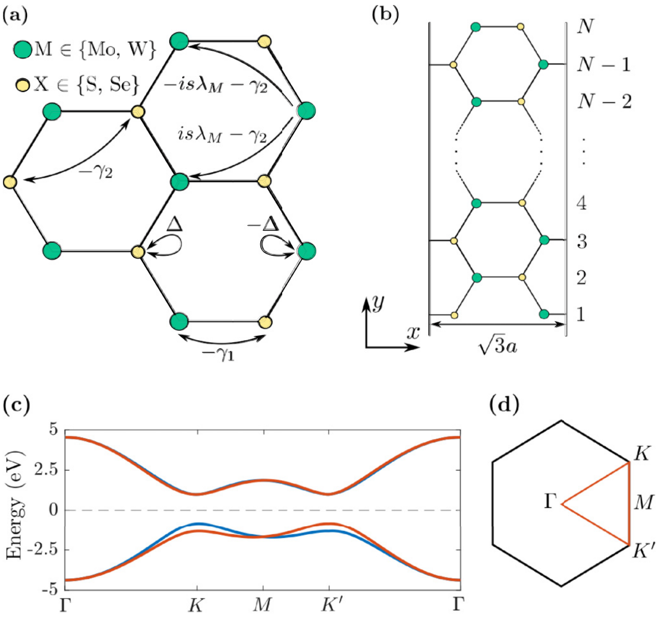

FIG. 1. (a) Schematic of the tight-binding couplings in the NNN-TB model for monolayer MX_2 TMDs. (b) Unit cell of a MX_2 armchair nanoribbon of width $(N-1)a/2$ and length $\sqrt{3}a$, where a is the lattice constant. (c) Band structure of $\mathrm{WSe_2}$ along the path in the Brillouin zone specified by the letters. The blue and red lines are the spin-up and spin-down bands, respectively. (d) Brillouin zone of monolayer TMD.

model and check convergence of the optical response. Finally, in Sec. IV, the magneto-optical response including excitons is studied using our nanoribbon model. In this section, we also calculate the diamagnetic shift of excitons in $\mathrm{WSe_2}$ and compare to recent experimental results.

II. SINGLE-PARTICLE PROPERTIES

In this section, we present the theoretical framework used to describe the single-particle properties of monolayer TMDs and nanoribbons. Two important characteristics of monolayer TMDs are the broken inversion symmetry and the strong spin-orbit coupling (SOC), which result in spin splitting of the conduction and valence band edge states [4,36–38]. In addition, TMDs also exhibit broken electron-hole symmetry, which leads to electrons and holes with different effective masses. To describe the single-particle properties of monolayer TMDs, we apply a tight-binding (TB) model. An orthogonal nearest-neighbor (NN) TB model always has electron-hole symmetry. Thus, in order to have different effective masses of electrons and holes, we need to use either a next-nearest-neighbor (NNN) model or include a finite overlap [31]. For this work, we have chosen to use a NNN TB model. The couplings used for a TMD with lattice constant a are illustrated in Fig. 1(a). Here, γ_1 and γ_2 are the NN and NNN hopping terms, respectively, and $-\Delta$ and Δ denote the on-site energies for transition metal (M) and chalcogen (X) atoms, respectively. Additionally, $is\lambda_M\eta$ is the SOC between NNN transition metal atoms, where $s=\pm 1$ denotes the spin and $\eta=\pm 1$ [39,40]. As shown for hBN systems in [39], the value of η depends on the rotation sense in a hexagon, $\eta=+1$ (-1) for clockwise (counterclockwise) orientation. This also holds for TMDs as they share the same point group as hBN [4,6,38]. For simplicity, we assume that the SOC between chalcogen atoms is negligible. The same couplings are used to describe both TMD monolayers and nanoribbons. Recently, a similar TB model was used in both the study of spin Hall effects in monolayer TMDs [40] and to compute the optical response of gapped and proximitized graphene [41].

We begin by considering a TMD monolayer placed in the xy plane. The couplings described above give the following two-band Hamiltonian for a state with wave vector $\mathbf{k}$:

$$\hat{H}=\begin{bmatrix}\Delta-\gamma_2 h & -\gamma_1 f\\ -\gamma_1 f^* & -\Delta-s\lambda_M g-\gamma_2 h\end{bmatrix}, \tag{1}$$

where

$$f(\mathbf{k})=e^{ik_xa/\sqrt{3}}+2e^{-ik_xa/2\sqrt{3}}\cos(k_ya/2), \tag{2}$$

$$g(\mathbf{k})=2\left[\sin\left(\frac{k_xa\sqrt{3}}{2}+\frac{k_ya}{2}\right)-\sin(k_ya)\right.$$
$$\left.-\sin\left(\frac{k_xa\sqrt{3}}{2}-\frac{k_ya}{2}\right)\right], \tag{3}$$

$$h(\mathbf{k})=2\left[\cos\left(\frac{k_xa\sqrt{3}}{2}+\frac{k_ya}{2}\right)+\cos(k_ya)\right.$$
$$\left.+\cos\left(\frac{k_xa\sqrt{3}}{2}-\frac{k_ya}{2}\right)\right]. \tag{4}$$

To determine the hopping parameters γ_1 and γ_2, we fit to the effective masses of electrons and holes in monolayer TMDs extracted from first-principles calculations in Ref. [42]. When doing this, we can assume that $\lambda_M=0$. This holds since λ_M is small compared to the band gap and, consequently, using a finite λ_M would only give a small correction to the hopping terms. Then, the energy bands are given by

$$E_\pm(\mathbf{k})=\gamma_2 h(\mathbf{k})\pm\sqrt{\Delta^2+\gamma_1^2|f(\mathbf{k})|^2}. \tag{5}$$

By expanding $E_\pm(\mathbf{k})$ around the K point $(k_x,k_y)=2\pi(1/\sqrt{3},1/3)/a$ in the Brillouin zone [illustrated in Fig. 1(d)], we get the following relations between the hopping parameters and the effective masses:

$$\frac{3a^2\gamma_1^2}{8\Delta}+\frac{3a^2}{4}\gamma_2=\frac{\hbar^2}{2m_e^*}, \tag{6}$$

$$\frac{3a^2\gamma_1^2}{8\Delta}-\frac{3a^2}{4}\gamma_2=\frac{\hbar^2}{2m_h^*}. \tag{7}$$

Here, $m_{e(h)}^*$ is the effective electron (hole) mass and $\hbar$ is the reduced Planck constant. Solving for γ_1 and γ_2 in Eqs. (6) and (7) gives the hopping parameters. The spin-dependent band gaps at the K and K' points are given by $E_g=2\Delta\mp 3\sqrt{3}s\lambda_M$, where $+$ $(-)$ holds at the K (K') point. The value of the SOC parameter λ_M is determined by matching the split to the spin splitting of the valence band edge calculated in Ref. [42]. The resulting band structure for $\mathrm{WSe_2}$ is plotted in Fig. 1(c). In Table I, we provide the complete set of parameters used for monolayer TMDs in the present paper.

TABLE I. Model parameters for the four common TMDs. The on-site energy, lattice constants, and screening lengths r_0 are taken from Ref. [42]. The SOC strengths are calculated from the spin splitting in Ref. [42], and the tight-binding couplings γ_1 and γ_2 are found by fitting to the electron and hole effective masses of Ref. [42].

	Δ (eV)	γ_1 (eV)	γ_2 (meV)	λ_M (meV)	a (Å)	r_0 (Å)
MoS_2	1.24	1.498	8.2	14.4	3.18	44.3
$MoSe_2$	1.09	1.359	92.5	18.3	3.32	51.2
WS_2	1.22	1.661	−51.7	43.3	3.19	39.9
WSe_2	1.04	1.444	−43.6	48.5	3.32	46.2

We introduce the external magnetic field by transforming the hopping integrals according to the Peierls substitution [43], which is simply the transformation $t \mapsto t_{ij} = te^{i\phi_{ij}}$, where t is equal to either γ_1, γ_2, or λ_M. The Peierls phase ϕ_{ij} is given by

$$\phi_{ij} = \frac{e}{\hbar}\int_{\mathbf{R}_i}^{\mathbf{R}_j} \mathbf{A}\cdot d\mathbf{l}. \tag{8}$$

Here, e is the elementary charge, $\mathbf{R}_i$ and $\mathbf{R}_j$ denote the location of atoms at site i and j, respectively, and $\mathbf{A}$ is the magnetic vector potential, related to the magnetic field by $\mathbf{B} = \nabla \times \mathbf{A}$. We take the magnetic field to be given by $\mathbf{B} = B\hat{z}$, where B is the magnetic field strength. For 2D systems the phase factor evidently breaks the periodicity of the tight-binding Hamiltonian, but it can be restored by using a suitable magnetic supercell [44]. As mentioned in Sec. I, the relation between field strength and the supercell size makes the calculation of excitonic properties unfeasible for experimentally obtainable fields. Indeed, with the current methodology (TB + BSE) and computer power available, magnetoexcitonic calculations are limited to field strengths of several thousand teslas. However, for a nanoribbon system, which is finite in the y direction, the Landau gauge, $\mathbf{A} = -By\hat{x}$, does not affect the translation symmetry of the system [35]. Hence, no restrictions on the magnetic field strength and no magnetic supercell are required. This is the motivation for using nanoribbons as a tool to describe the magneto-optical response of monolayer TMDs for arbitrary magnetic field strengths. We will consider armchair nanoribbons, which are infinite in the x direction and have a finite width of $W = (N-1)a/2$, where N is the number of dimer lines in the y direction. The unit cell is illustrated in Fig. 1(b). Since the nanoribbon system is finite in the x direction, edge states are expected to exist for all nanoribbon widths [45]. In Appendix A, we check the convergence of the electronic structure by examining the density of states (DOS). The edge states are found to have negligible effect on the electronic structure for $N \gtrsim 200$. Consequently, by increasing N, we expect the optical response of the nanoribbons to converge to that of the 2D system.

To calculate the linear optical conductivity, we make use of the following expression for the spin-up and spin-down contribution to the linear optical conductivity [33],

$$\sigma^s_{\alpha\beta}(\omega) = -\frac{ie^2\hbar^2\omega}{m^2A}\sum_{cvk}\frac{p^{\alpha}_{cvk,s}p^{\beta}_{vck,s}}{E^2_{cvk,s}(E_{cvk,s}-\hbar\omega-i\hbar\Gamma)}, \tag{9}$$

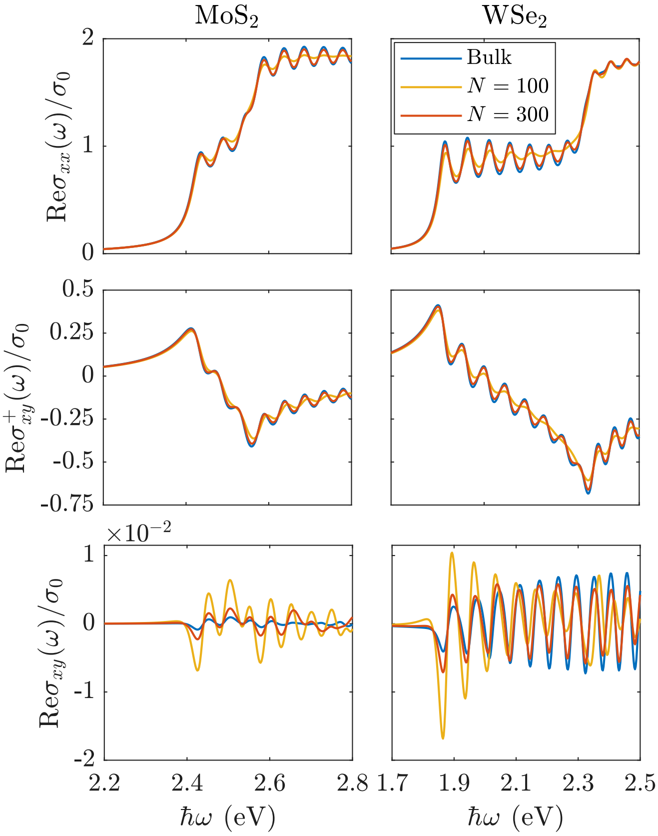

FIG. 2. Single-particle linear optical conductivities versus photon energy. The spectra are calculated for $B = 130$ T and $\hbar\Gamma = 25$ meV. The factor of 10^{-2} should be multiplied with the y axis directly underneath. The blue lines refer to the 2D conductivities and red and yellow lines to the nanoribbon case.

with $\alpha, \beta \in \{x, y\}$, $\hbar\omega$ the photon energy, $\hbar\Gamma$ a phenomenological broadening parameter, m the free electron mass, $A = WL$ the system area, where W is the system width and L is the system length, $p^{\alpha}_{cvk,s}$ the momentum matrix elements, and $E_{cvk,s} := E_c(k,s) - E_v(k,s)$ the transition energy. The sum runs over all combinations of conduction (c) and valence (v) bands and k points, and we have neglected the nonresonant term of the conductivity. In the nanoribbon geometry, the limit where L goes to infinity should be taken. In practice this is done by converting the sum over k points to an integral by using that the distance between two k points is equal to $\Delta k = 2\pi/L$. The linear optical conductivity tensor elements are then found by summing over spin, i.e., $\sigma_{\alpha\beta}(\omega) = \sigma^+_{\alpha\beta}(\omega) + \sigma^-_{\alpha\beta}(\omega)$. By symmetry, we have the relation $\sigma^+_{\alpha\alpha}(\omega) = \sigma^-_{\alpha\alpha}(\omega)$ for the diagonal elements, and $\sigma^+_{\alpha\beta}(\omega) = -\sigma^-_{\alpha\beta}(\omega)$ for the off-diagonal elements when $B = 0$ T. We note that the expression in Eq. (9) holds for both nanoribbons and 2D monolayers, but k denotes a scalar quantity in the former case and a vector quantity in the latter case.

In Fig. 2, we show the real part of the optical conductivity in the single-particle approximation for 2D monolayers and nanoribbons. All spectra are plotted in units of $\sigma_0 = e^2/4\hbar$ and calculated for a Brillouin zone discretized using 120 k points. In the particular case of Fig. 2, we plot the spectra with a broadening of 25 meV. This value is used in order to clearly show the different features of the optical response and how they converge. Throughout, we focus on MoS_2 and WSe_2 as examples of monolayer TMDs, but similar results hold for other types of TMDs. In Fig. 2, the spectra are computed for a very strong magnetic field to make it possible to distinguish the peaks due to Landau levels (LLs). The LLs are clearly visible in both the diagonal and off-diagonal response. The plots also illustrate the finite off-diagonal conductivities, the so-called Hall conductivities, present when there is an external magnetic field. Comparing the response of the $N = 100$ and $N = 300$ nanoribbons to the bulk conductivity, we see that for $\sigma_{xx}(\omega)$ and $\sigma_{xy}^{+}(\omega)$ both nanoribbon widths capture the qualitative features. However, the wider nanoribbons more accurately capture the position of the higher Landau levels and the amplitudes of the peaks. In contrast, for $\sigma_{xy}(\omega)$ very wide nanoribbons are needed to obtain good convergence of the amplitudes. This is due to the fact that $\sigma_{xy}(\omega)$ is the sum of $\sigma_{xy}^{+}(\omega)$ and $\sigma_{xy}^{-}(\omega)$, both of which are much bigger in amplitude than $\sigma_{xy}(\omega)$. Thus, while the difference between the spin-dependent off-diagonal response of nanoribbons and 2D is small compared to the amplitude of $\sigma_{xy}^{+}(\omega)$ it is large compared to the amplitude of the Hall conductivity—consequently, making the Hall conductivity susceptible to poor convergence. The excitonic spectra are expected to show better convergence since the optical response is dominated by excitons and the excitons are strongly localized in TMDs [7,8,46]. Finally, we note that the valley Zeeman splitting is not described by the TB Hamiltonian in this paper.

III. EXCITONIC EFFECTS

In this section, we include excitonic effects in our description of TMD monolayers and nanoribbons. The approach follows that of Refs. [35,47]. We expand the excitonic wave function $|exc\rangle$ in a basis of singlets formed by excitations between a single pair of spin-dependent valence and conduction bands at k, such that the wave function is given by

$$|exc\rangle = \sum_{cvk,s} A^{s}_{cvk} |vks \rightarrow cks\rangle, \tag{10}$$

where A^{s}_{cvk} are the expansion coefficients and $|vks \rightarrow cks\rangle$ the singly excited states. Note that we only include excitations between bands of equal spin and that k can be either a vector or scalar quantity depending on the dimensionality of the system under consideration. The excitonic states are governed by the Bethe-Salpeter equation (BSE) [7], which for the expansion in Eq. (10) take the form

$$E_{cvk,s} A^{s}_{cvk} + \sum_{c'v'k',s'} W^{s,s'}_{cvk,c'v'k'} A^{s'}_{c'v'k'} = E A^{s}_{cvk}. \tag{11}$$

Here, $W^{s,s'}_{cvk,c'v'k'}$ is the electron-hole interaction matrix elements and E is the exciton energy. Note that we have neglected the exchange term in the BSE for simplicity. Then, the electron-hole interaction matrix elements are given by

$$W^{s,s'}_{cvk,c'v'k'} = \langle vks \rightarrow cks|U|v'k's' \rightarrow c'k's'\rangle, \tag{12}$$

where U is the electron-hole interaction potential defined below. Performing the spin integral in Eq. (12), we find

$$W^{s,s'}_{cvk,c'v'k'} = \delta_{s,s'} \iint d^3\mathbf{r} d^3\mathbf{r}' \phi^{*}_{cks}(\mathbf{r}) \phi_{vks}(\mathbf{r}') \times U(\mathbf{r} - \mathbf{r}') \phi_{c'k's}(\mathbf{r}) \phi^{*}_{v'k's}(\mathbf{r}'). \tag{13}$$

Here, $\phi_{\alpha k s}(\mathbf{r})$ are the tight-binding states with $\alpha \in \{c, v\}$. Equation (13) shows that the spin-up and spin-down equations decouple and can be solved independently.

In a strict 2D system the electron-hole interaction is not the usual Coulomb potential, but instead modeled by the Keldysh potential [48,49],

$$U(\mathbf{r}) = -\frac{e^2}{8\varepsilon_0 r_0} \left[H_0\left(\frac{\kappa r}{r_0}\right) - Y_0\left(\frac{\kappa r}{r_0}\right) \right]. \tag{14}$$

Here, ε_0 is the vacuum permittivity, H_0 and Y_0 are Struve and Neumann functions, respectively, $r = |\mathbf{r}|$, r_0 is an in-plane screening length, and κ is the average of the relative dielectric constant of the substrate and capping material. The values of r_0 used in this paper are listed in Table I. For the strict 2D system, a straightforward calculation of the matrix elements in Eq. (13) can be done using the approach of Ref. [47]. For the nanoribbon geometry, additional considerations are needed. We want the excitonic properties in the nanoribbon geometry to converge to those of the 2D system, when the ribbon width is sufficiently large. Thus, we need to modify the approach of Ref. [47] to work for structures, which are periodic in one direction, but have non-negligible width. The details are provided in Appendix B, but the main result is that for the nanoribbon geometry the matrix elements $W^{s,s}_{cvk,c'v'k'}$ can be computed from

$$W^{s,s}_{cvk,c'v'k'} = \sum_{n,m} I^{n,s}_{ck,c'k'} I^{m,s}_{v'k',vk} U^{k,k'}_{n,m}. \tag{15}$$

Here n and m run over the atomic sites in the unit cell and $I^{n,s}_{\alpha k,\beta k'} = C^{n*}_{\alpha k s} C^{n}_{\beta k' s}$ is the Bloch overlap given by the product of the tight-binding eigenvector elements belonging to site n. Finally, the integral factor $U^{k,k'}_{n,m}$ is defined as

$$U^{k,k'}_{n,m} = -\frac{e^2}{2\pi L \varepsilon_0} \int_0^\infty dz K_0\left(\sqrt{r_0^2 z^2 + Y_{nm}^2} |k - k'|\right) e^{-\kappa z}, \tag{16}$$

where K_0 is a modified Bessel function of the second kind and $Y_{nm} = Y_n - Y_m$ is the difference between the y coordinates of the atoms belonging to orbitals n and m. The integral in Eq. (16) is computed numerically using a suitable Gauss quadrature.

The eigenvalue problem defined in Eq. (11) can be solved by diagonalization. Due to the decoupling of spin-up and spin-down equations, the matrix to be diagonalized is block diagonal. Thus, to obtain the full solution two eigenvalue problems of dimension $N_c N_v N_k$ have to be solved. Here, N_c and N_v are the number of conduction and valence bands, respectively, and N_k is the number of k points. For a magnetic field of 100 T the 2D magnetic supercell consists of roughly 2000 atoms, hence making diagonalization of the BSE problem computationally unfeasible. On the other hand, using nanoribbons as a theoretical tool the linear optical response converges to the bulk

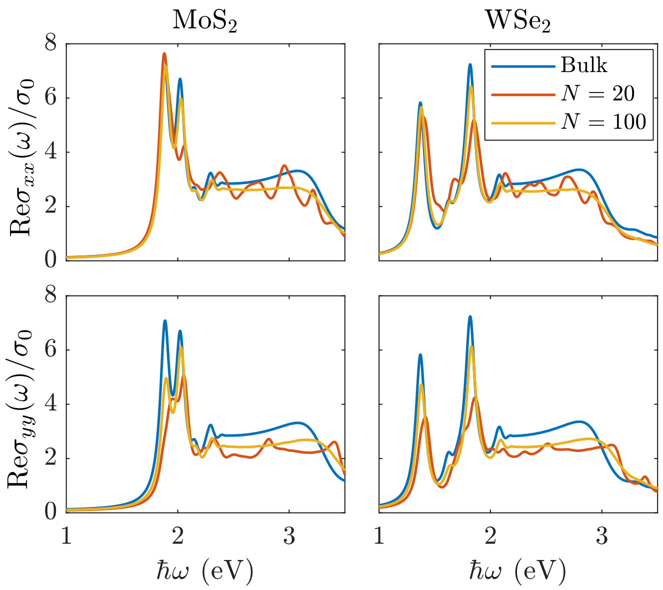

FIG. 3. Many-body diagonal conductivities versus photon energy, calculated for $B = 0$ T, $\hbar\Gamma = 50$ meV, and $\kappa = 1$. The blue lines refer to the 2D conductivities and yellow and red lines to the nanoribbon spectra.

2D response when the nanoribbon unit cell contains roughly 200 atoms. The result is that the computations are feasible, although still very demanding. However, if only the optical response and not the full eigenvalue decomposition is needed a significant reduction in computational complexity can be obtained by using the Lanczos approach in Refs. [35,47].

The Lanczos routine is based on the fact that the real part of the linear optical conductivity can be computed from the expression [47]

$$\mathrm{Re}\sigma_{\alpha\beta}(\hbar\omega) = -\frac{e^2}{m^2\omega A}\sum_s \mathrm{Im}\langle P_{\alpha s}|\hat{G}_s(\hbar\omega)|P_{\beta s}\rangle, \tag{17}$$

with $\alpha, \beta \in \{x, y\}$, $\hat{G}_s(\hbar\omega)$ the many-body Green's function given below, and $P_{\alpha s}$ given by

$$|P_{\alpha s}\rangle := \hat{P}_\alpha|0, s\rangle = \sqrt{2}\sum_{cvk} A^s_{cvk}\, p^\alpha_{cvk,s}. \tag{18}$$

Here, $|0, s\rangle$ is the many-body ground state, $\hat{P}_\alpha$ is the many-body momentum operator, and $p^\alpha_{cvk,s}$ denote the single-particle momentum matrix elements. The many-body Green's function in Eq. (17) is given by

$$\hat{G}_s(\hbar\omega) = \lim_{\hbar\Gamma\to 0^+}(\hbar\omega + i\hbar\Gamma - \hat{H}_s)^{-1}, \tag{19}$$

where $\hat{H}_s$ is the many-body Hamiltonian. In practice, we allow a small, finite $\hbar\Gamma$ to add broadening to the spectra. The matrix elements of the Green's function in Eq. (17) are evaluated effectively as in Ref. [35], i.e., using the Lanczos-Haydock routine for tridiagonalization [50]. Computationally this is still a daunting task due to the size of the problem. For a nanoribbon with $N = 100$ and using a discretization with $N_k = 120$, the matrix that is to be tridiagonalized has dimension $(1.2 \times 10^6) \times (1.2 \times 10^6)$. We reduce the size of the problem by disregarding the top and bottom half of the conduction and valence bands, respectively, which primarily affect the high-energy part of the spectra.

In Fig. 3, we show the convergence of the nanoribbon conductivities to the 2D response in the unperturbed case ($B = 0$). The two main exciton peaks at 1.88 eV and 2.02 eV for MoS$_2$ and at 1.37 eV and 1.82 eV for WSe$_2$ are denoted by A and B, respectively. The results show a good convergence for the nanoribbon with $N = 100$. Both the A and B exciton peaks coincide with the bulk results and the peaks corresponding to the excited states also match the bulk results. The discrepancy at high photon energies is due to our disregarding some bands in the excitonic calculations. Regarding the amplitude of the peaks, we see that the amplitude is close to the bulk result for Reσ_{xx}, while the Reσ_{yy} results could be improved by using wider nanoribbons. However, as our goal is to study the effect of an external magnetic field on the optical response, the convergence shown in Fig. 3 is satisfactory. Comparing to the spectra of unperturbed TMDs in Ref. [9], we see that the qualitative features agree well.

IV. RESULTS

In this section, we present the results obtained from the theoretical framework of Secs. II and III. All calculations are based on the nanoribbon geometry and are calculated for nanoribbons with $N = 100$. This corresponds to a ribbon width of 15.7 nm and 16.4 nm for MoS$_2$ and WSe$_2$, respectively. The one-dimensional Brillouin zone is discretized using 120 k points. For the spectra in this section, a broadening of $\hbar\Gamma = 50$ meV is used, which is at the high end of experimentally measured broadenings [51–53]. However, this value is needed in order to remove artifacts caused by the finite width of the system. The framework described in Sec. III is based on the assumption that the temperature is 0 K. However, as the thermal energy at room temperature ($\approx$25 meV) is smaller than the broadening, the band gap, and the exciton binding energy, we expect the spectra presented here to be good approximations at room temperature. It should be noted that the band gap tends to decrease with temperature. Consequently, the spectra should be shifted accordingly for comparison with room-temperature measurements.

The results presented in this paper are for magnetic field strengths of 10, 30, 65, and 130 T. Currently, measurements of magneto-optical properties of TMDs have been performed in fields up to 65 T and, thus, most of the results presented here are experimentally verifiable [24,27,28]. Moreover, destructive pulsed magnets can deliver fields as high as 130 T [54]. Another interesting approach is to study TMDs placed on a magnetic substrate. This has been shown to induce exchange fields in the TMD monolayer equivalent to extremely high magnetic fields [55,56].

In Fig. 4, the first row of plots shows the change of the real part of the diagonal conductivity as a function of the magnetic field strength relative to the zero-field case. To illustrate this, we have plotted the difference between the diagonal conductivity at a finite magnetic field strength and at 0 T. The plots show that the exciton peaks in MoS$_2$ and WSe$_2$ exhibit a small blueshift in response to the applied magnetic field. This small but important phenomena is what allows for experimental estimation of the spatial extent and

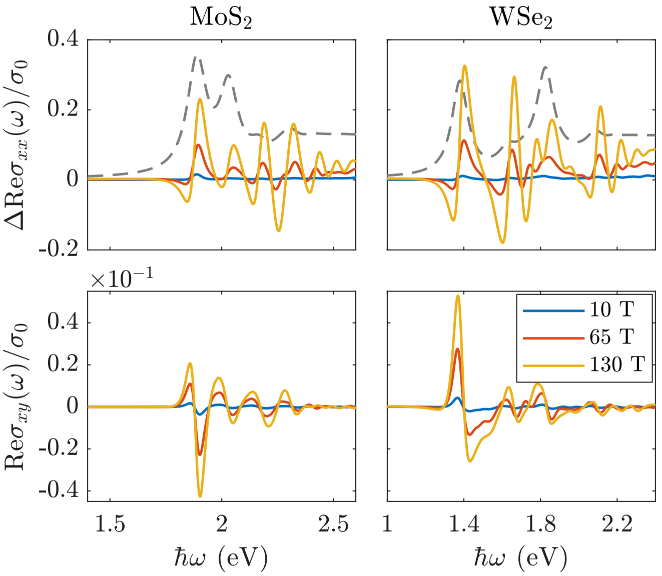

FIG. 4. Excitonic optical conductivity versus photon energy, for different magnetic field strengths. The first row illustrates $\Delta\mathrm{Re}\sigma_{xx}(\omega)$, which is the difference between the diagonal conductivity at a finite magnetic field strength and at 0 T. The dashed gray lines show the unperturbed spectra. The second row shows the Hall conductivities at different magnetic field strengths. Spectra are for nanoribbons with $N = 100$ and $\kappa = 1$. The factor 10^{-1} should be multiplied with the y axis directly underneath.

effective mass of excitons. We will evaluate the size of the shift and discuss this in detail below. In addition to the blueshift of the peaks, the amplitudes also increase slightly as the field strength increases. Comparing to the amplitude of the peaks in the unperturbed spectra in Fig. 3, the increase in amplitude due to the magnetic field is only a few percent for a field strength of 130 T. Thus, both effects are small changes relative to the unperturbed results. Finally, in the high-energy part of the spectra, the results show the emergence of an oscillating modulation appearing at strong magnetic fields. These oscillations correspond to transitions between Landau levels.

The second row of plots in Fig. 4 shows the Hall conductivities of MoS$_2$ and WSe$_2$. Similarly to the single-particle case, the time-reversal symmetry present in the absence of an external magnetic field ensures that the unperturbed excitonic Hall conductivities vanish identically; that is, $\sigma_{xy}(B=0)=0$. Consequently, they are not shown in Fig. 4. When time-reversal symmetry is broken by the external magnetic field, finite Hall conductivities are found even at small magnetic field strengths. Thus, we have $\sigma_{xy}(B>0)\neq 0$. In other words, the Hall conductivity goes from being identically zero to having a finite magnitude when the magnetic field is turned on. Hence, the relative change of the Hall conductivities is very significant. In contrast, the relative change of the diagonal conductivity is only minor, as $\sigma_{xx}(B>0)/\sigma_{xx}(B=0)\approx 1$. Comparing the excitonic magneto-optical response in Fig. 4 to the IPA results in Fig. 2, we see that excitonic effects change the optical response significantly. In addition to changing the overall shape of the spectra, we also see that the excitonic Hall conductivities are approximately one order of magnitude larger than the IPA response. Hence, for an accurate description of the magneto-optical properties of monolayer TMDs, it is clearly important to account for excitons. Regarding the magnetic field dependence of the Hall conductivities in Fig. 4, we see that the amplitude scales linearly with the magnetic field strength. However, as we go to stronger fields, small changes in the shape of the spectra occur. These changes are due to the emergence of Landau levels and additional effects that are nonlinear in B, such as the diamagnetic shift.

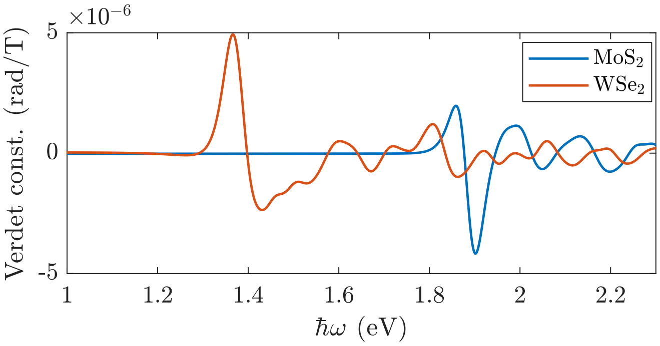

FIG. 5. Plot of the Verdet constant versus photon energy for normal incident light on a TMD monolayer in vacuum.

The finite Hall conductivity, present when there is an external magnetic field, causes the system to exhibit a magneto-optical Kerr effect (MOKE) and a Faraday effect. The MOKE is a rotation of the polarization state of light when reflected off the surface of a magnetized material, while the Faraday effect is a rotation of the polarization of the transmitted light. Here, we compute the Faraday rotation angle θ for normal incidence of light on a single layer of TMD. The rotation angle for a single passage of the monolayer can be approximated by [32,57]

$$\theta = \frac{1}{(n_1+n_2)c\varepsilon_0}\mathrm{Re}\sigma_{xy}(\omega), \tag{20}$$

where n_1 and n_2 are the refractive index of the substrate and capping material, respectively, and c is the speed of light. The expression in Eq. (20) is valid when $\sigma_{xx}\gg\sigma_{xy}$. As the Hall conductivity scales linearly with B at small field strengths, the Faraday rotation angle is often expressed as $\theta = VB$, where V is the so-called Verdet constant [31]. In Fig. 5, we have computed the Verdet constant for freestanding MoS$_2$ and WSe$_2$. As shown by the figure, the rotation for a single passage of the TMD monolayer is very small. However, this could be increased by placing the monolayer in an optical cavity in order to enhance the rotation by multiple passes [57,58].

As mentioned in Sec. III, the electron-hole interaction is screened by the substrate and capping materials. This screening is described by the κ parameter, which is simply the average of the relative dielectric constant of the substrate and capping material. In Fig. 6, the optical conductivity of WSe$_2$ is shown for κ values of 1, 1.55, and 4.5. These values correspond to WSe$_2$ placed in vacuum, on a SiO$_2$ substrate, or encapsulated in hBN, respectively [27,59]. It should be noted that an exchange self-energy correction to the single-particle band gap exists, and this effect is not included in our

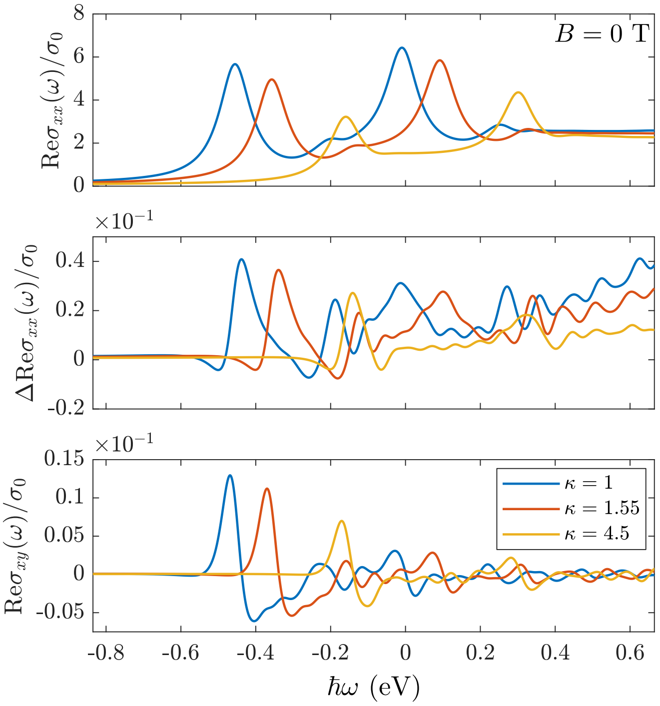

FIG. 6. Excitonic optical conductivity versus photon energy, calculated for WSe_2 in different dielectric environments. The top panel shows the diagonal conductivity in the unperturbed case. The middle panel shows the change in the diagonal conductivity from the unperturbed case to the $B = 30$ T case. The bottom panel shows the Hall conductivities calculated at $B = 30$ T. The factors of 10^{-1} should be multiplied with the y axes directly underneath.

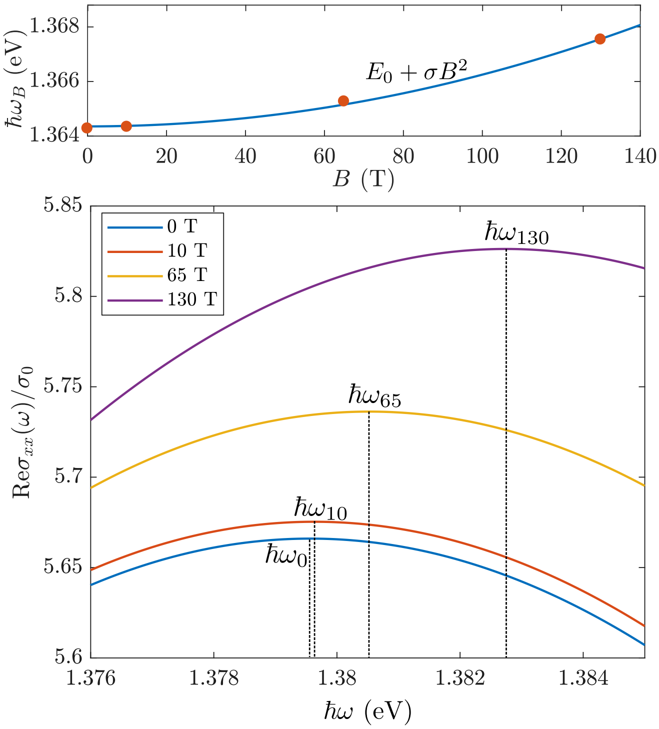

FIG. 7. Diamagnetic shift of the peak associated with the 1s state of the A exciton in WSe_2. The vertical dashed lines indicate the peak position at different magnetic field strengths. The upper panel illustrates the fit of the function $E_0 + \sigma B^2$ (blue line) to the peak positions marked by the red dots.

simple model. The self-energy correction decreases when the screening from the surroundings increases [29,34]. To account for this missing effect, the spectra in Fig. 6 are shifted by the band gap energy. This allows us to observe changes in exciton binding energy as a function of κ. The first plot is of the diagonal conductivity for $B = 0$ T, and the results show a blueshift of the exciton peaks as κ increases. This is due to a decrease in the exciton binding energy as the screening from the surroundings is increased. The binding energy decreases from 455 meV to 160 meV as κ increases from 1 to 4.5. The second row shows the change in the diagonal conductivity between the unperturbed case and the $B = 30$ T case. The plots show that the diamagnetic shift of the 2s exciton states becomes harder to observe at higher values of κ, and that the Landau levels are not affected by the dielectric environment. Finally, the last plot is of the Hall conductivities. Here, the same blueshift is observed as in the diagonal conductivity. When going to the limit $\kappa \to \infty$, we recover the IPA results, as has been checked numerically.

In the low-field limit, the magnetic field dependence of the energy of s-type excitons can be described by the relation $E_B \approx E_0 + \sigma B^2$, where E_0 is the unperturbed exciton energy and σ is the diamagnetic shift coefficient. The quadratic diamagnetic shift of the exciton peaks is illustrated in Fig. 7 for the A exciton in WSe_2. This coincides precisely with the small shift observed in the diagonal conductivities in Fig. 4. As mentioned, the value of σ is related to the spatial extent of the exciton. The relation is given by $\sigma = e^2\langle r^2\rangle/8\mu$, where $\sqrt{\langle r^2\rangle}$ is the root-mean-square (rms) radius of the exciton and μ is the reduced exciton mass. If μ is known, this relation allows for an experimental estimate of the exciton size. As the Lanczos method only provides the optical conductivity, and not the exciton energies, we compute the shift coefficient by following the exciton peak in the spectra as the field strength changes. The shift of the exciton peak is then fitted to a parabola, and the diamagnetic shift coefficient is found. Doing this for the A exciton peak of freestanding WSe_2, we find a σ value of 0.22 μeV/T^2. Using the same effective masses as applied to find the TB parameters, we find an rms radius of 1.52 nm for the A exciton.

The dielectric environment is expected to affect the size of the diamagnetic shift. Increasing κ results in less tightly bound excitons, thus having a larger radius. This consequently results in larger diamagnetic shift coefficients. This effect was studied experimentally in Ref. [27]. In Table II, we summarize our findings with regard to the effect of the dielectric environment on the diamagnetic shift coefficient. We have also included values computed from the Wannier model presented in Ref. [29]. The Wannier model consistently underestimates σ, when comparing to the experimental values and the values computed using the nanoribbon approach. The explanation for this is found in the fact that the Bloch overlaps are disregarded in the Wannier model. This causes the excitons to be more strongly bound in the Wannier framework than in BSE framework and, consequently, have smaller diamagnetic shift coefficients. This shows the importance of including the

TABLE II. Calculated and experimental values of σ in units of μeV/T^2 for the 1s state of the A exciton in WSe$_2$. The first column gives the values calculated using the approach presented in this paper, while the second column gives the values calculated using the Wannier model from Ref. [29]. The κ values of 2.25 and 3.30 correspond to TMDs on a SiO$_2$ substrate capped by polybisphenol carbonate and hBN, respectively [27].

κ	σ (BSE)	σ (Wannier)	σ (Expt.)
1.00	0.22	0.13	
1.55	0.24	0.15	0.18 [27]
2.25	0.27	0.17	0.25 [27]
3.30	0.31	0.19	0.32 [27]
4.50	0.36	0.23	0.24 [26], 0.31 [24]

Bloch overlaps when modeling magnetoexcitons. Comparing the diamagnetic coefficients calculated using the nanoribbon approach to the experimental results, we observe a better agreement.

V. SUMMARY

In summary, we have used nanoribbons as a theoretical tool for the study of the magneto-optical response of monolayer TMDs. We have shown that by increasing the width of the nanoribbons the optical response will converge to that of a 2D monolayer. This has proven to be useful for including excitonic effects in the calculation of the magneto-optical response of TMDs, since a strict 2D calculation is not currently feasible. Beginning from a simple tight-binding model, we added excitonic effects in the framework provided by the Bethe-Salpeter equation. The linear optical conductivity was calculated effectively using the Lanczos-Haydock routine. We found that a 15–16 nm wide nanoribbon system is sufficient for a reasonable convergence of the optical response.

Using this approach, we are able to compute the excitonic Hall conductivity of monolayer TMDs. The calculated Hall conductivity spectra can be used to compute Faraday rotation in monolayer TMDs, an important magneto-optical effect. We also evaluated the diamagnetic shift coefficient, which provides a useful quantity for evaluating the size of excitons. So far, the experimentally determined diamagnetic shift coefficients have only been compared to theoretical results based on effective mass models. But our approach provides the option of going beyond effective mass models when analyzing experimental data. We compared the theoretical diamagnetic shift coefficient given by our calculation to values calculated using a Wannier model and to recent experimentally determined coefficients. The comparison with the values computed from the Wannier model showed the importance of including Bloch overlaps, while the comparison with experimental values showed a very good agreement between our calculations and the experimental results.

Finally, another potential use of the approach presented in this paper is as a benchmark for future strict 2D models. As it is currently not possible to compute the excitonic Hall conductivities in any 2D model, the Hall conductivity presented here can provide a reference when attempting to develop new models.

ACKNOWLEDGMENTS

J.H. and T.G.P. gratefully acknowledge financial support by the QUSCOPE Center, sponsored by the Villum Foundation. Additionally, T.G.P. is supported by the Center for Nanostructured Graphene (CNG), which is sponsored by the Danish National Research Foundation, Project No. DNRF103. N.M.R.P. acknowledges support from the European Commission through the project "Graphene-Driven Revolutions in ICT and Beyond" (Ref. No. 785219), COMPETE2020, PORTUGAL2020, FEDER, and the Portuguese Foundation for Science and Technology (FCT) through project POCI-01-0145-FEDER-028114 and in the framework of the Strategic Financing UID/FIS/04650/2013.

APPENDIX A: CONVERGENCE

In this Appendix, we examine the convergence of the electronic properties of the nanoribbon system. We need to ensure that the effect of edge states in the nanoribbon system is negligible. This is done by studying the DOS of the nanoribbons and comparing to that of the 2D system. The DOS is defined as

$$D(E) = \frac{1}{A}\sum_{\alpha,s,k}\delta(E - E_\alpha(k,s)), \tag{A1}$$

where α runs over all bands. In practice, the δ function in the DOS is approximated by a Lorentzian with 25 meV broadening.

In Fig. 8 the convergence of the nanoribbon DOS is illustrated. For nanoribbons with $N = 50$ and $N = 100$, oscillations in the DOS due to the finite width of the system are observed. In contrast, the DOS of the larger nanoribbons with $N = 200$ and $N = 300$ are almost identical to the 2D DOS except for two small small peaks around -3.3 and 3.5 eV. One of the peaks is illustrated in the inset in Fig. 8. The peaks corresponds to edge states in the nanoribbon system and, as we have checked numerically, will remain a feature of the nanoribbon DOS independently of the ribbon width. However, the photon energy needed for transitions from an edge state to a bulk state is approximately 4.3 eV (the energy difference between the valence edge states to the bottom of the conduction

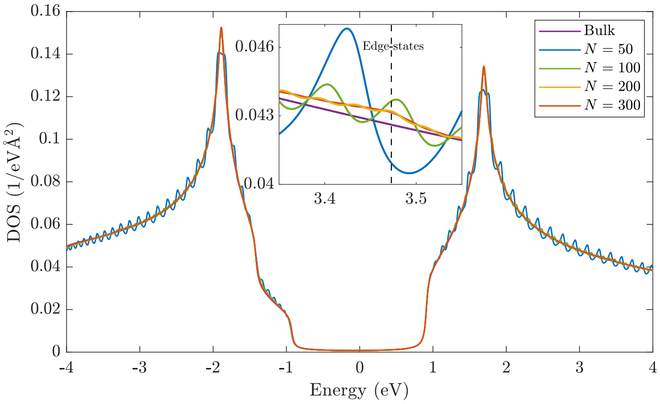

FIG. 8. DOS versus energy for WSe$_2$ plotted for a 2D monolayer and different nanoribbon widths. The inset shows a zoom of the DOS in the vicinity of the conduction edge states around 3.47 eV.

band). Consequently, edge states will not affect the optical response in the photon range considered in the present work.

APPENDIX B: ELECTRON-HOLE INTERACTION MATRIX ELEMENTS FOR NANORIBBONS

In this Appendix, we will find an expression for the matrix elements in Eq. (13) for the nanoribbon geometry. We begin by considering the product of two tight-binding states, such as the ones in Eq. (13). Exploiting the fact that the atomic orbitals are localized and orthogonal, we can write

$$\phi^*_{\alpha k s}(\mathbf{r})\phi_{\beta k' s}(\mathbf{r}) \approx \frac{1}{N_{uc}}\sum_{n,X} I^{n,s}_{\alpha k,\beta k}\, e^{i(k'-k)X}\varphi_n^2(\mathbf{r}-X\hat{x}), \quad \text{(B1)}$$

where N_{uc} is the number of unit cells, X is the location of the unit cell in the periodic direction, $I^{n,s}_{\alpha k,\beta k} = C^{n*}_{\alpha k s}C^{n}_{\beta k' s}$ are the products of the tight-binding eigenvector elements belonging to the nth atomic orbital, and φ_n are the atomic orbitals. The X sum runs over the location of the unit cells in the periodic direction. To evaluate the matrix elements, we need integrals of the form

$$U_{n,m}(X,X') = \iint \varphi_n^2(\mathbf{r}-X\hat{x})\,U(\mathbf{r}-\mathbf{r}')\,\varphi_m^2(\mathbf{r}'-X'\hat{x})\,d^3\mathbf{r}\,d^3\mathbf{r}'. \quad \text{(B2)}$$

For strongly localized atomic orbitals, we can assume the effective interaction

$$\begin{aligned} U_{n,m}(X,X') &\approx U^{\rm eff}_{n,m}(X-X') \\ &\equiv -\frac{e^2}{8\varepsilon_0 r_0}\left[H_0\left(\frac{\kappa\sqrt{(X-X')^2+Y^2_{nm}}}{r_0}\right)\right. \\ &\quad \left. - Y_0\left(\frac{\kappa\sqrt{(X-X')^2+Y^2_{nm}}}{r_0}\right)\right]. \end{aligned} \quad \text{(B3)}$$

Here, Y_{nm} denotes the difference in y coordinates of the atomic site belonging to orbitals n and m. This effective interaction is validated by its ability to recover the 2D results, as shown in the paper. In the following, it is advantageous to rewrite $U^{\rm eff}_{n,m}(X-X')$ using an integral form of the Keldysh potential [60]. This gives

$$U^{\rm eff}_{n,m}(X-X') = -\frac{e^2}{4\pi\varepsilon_0}\int_0^\infty \frac{1}{\sqrt{(r_0 z)^2+(X-X')^2+Y^2_{nm}}}\, e^{-z\kappa}\,dz. \quad \text{(B4)}$$

The interaction matrix elements in Eq. (13) can then be approximated by

$$W^{s,s'}_{cvk,c'v'k'} \approx \delta_{s,s'}\sum_{n,m} I^{n,s}_{ck,c'k'} I^{m,s}_{v'k',vk}\,\frac{1}{L}\int e^{i(k'-k)X}\,U^{\rm eff}_{n,m}(X)\,dX, \quad \text{(B5)}$$

where we have converted the sum over X to an integral and L denotes the length of the system. Finally, we have to do the X integration, which corresponds to taking the Fourier transform of the effective interaction. This gives

$$\begin{aligned} &\frac{1}{L}\int e^{i(k'-k)X}\,U^{\rm eff}_{n,m}(X)\,dX \\ &\quad = -\frac{e^2}{2\pi L\varepsilon_0}\int_0^\infty dz\,K_0\left(\sqrt{r_0^2 z^2+Y^2_{nm}}\,|k-k'|\right)e^{-\kappa z}, \end{aligned} \quad \text{(B6)}$$

where K_0 denotes a modified Bessel function of the second kind. The remaining integral over z can be evaluated numerically. Inserting Eq. (B6) into Eq. (B5), we obtain an expression for the interaction matrix elements in the nanoribbon geometry.

[1] K. F. Mak, C. Lee, J. Hone, J. Shan, and T. F. Heinz, Phys. Rev. Lett. **105**, 136805 (2010).

[2] A. Splendiani, L. Sun, Y. Zhang, T. Li, J. Kim, C.-Y. Chim, G. Galli, and F. Wang, Nano Lett. **10**, 1271 (2010).

[3] Y. Zhang, T.-R. Chang, B. Zhou, Y.-T. Cui, H. Yan, Z. Liu, F. Schmitt, J. Lee, R. Moore, Y. Chen *et al.*, Nat. Nanotechnol. **9**, 111 (2014).

[4] D. Xiao, G.-B. Liu, W. Feng, X. Xu, and W. Yao, Phys. Rev. Lett. **108**, 196802 (2012).

[5] X. Xu, W. Yao, D. Xiao, and T. F. Heinz, Nat. Phys. **10**, 343 (2014).

[6] G.-B. Liu, W.-Y. Shan, Y. Yao, W. Yao, and D. Xiao, Phys. Rev. B **88**, 085433 (2013).

[7] T. C. Berkelbach, M. S. Hybertsen, and D. R. Reichman, Phys. Rev. B **88**, 045318 (2013).

[8] M. M. Ugeda, A. J. Bradley, S.-F. Shi, H. Felipe, Y. Zhang, D. Y. Qiu, W. Ruan, S.-K. Mo, Z. Hussain, Z.-X. Shen *et al.*, Nat. Mater. **13**, 1091 (2014).

[9] A. Chaves, R. Ribeiro, T. Frederico, and N. Peres, 2D Mater. **4**, 025086 (2017).

[10] M. Van der Donck, M. Zarenia, and F. M. Peeters, Phys. Rev. B **97**, 195408 (2018).

[11] Z. Wang, J. Shan, and K. F. Mak, Nat. Nanotechnol. **12**, 144 (2017).

[12] F. Rose, M. O. Goerbig, and F. Piéchon, Phys. Rev. B **88**, 125438 (2013).

[13] R.-L. Chu, X. Li, S. Wu, Q. Niu, W. Yao, X. Xu, and C. Zhang, Phys. Rev. B **90**, 045427 (2014).

[14] Y. Li, J. Ludwig, T. Low, A. Chernikov, X. Cui, G. Arefe, Y. D. Kim, A. M. van der Zande, A. Rigosi, H. M. Hill *et al.*, Phys. Rev. Lett. **113**, 266804 (2014).

[15] D. MacNeill, C. Heikes, K. F. Mak, Z. Anderson, A. Kormányos, V. Zólyomi, J. Park, and D. C. Ralph, Phys. Rev. Lett. **114**, 037401 (2015).

[16] A. Srivastava, M. Sidler, A. V. Allain, D. S. Lembke, A. Kis, and A. Imamoğlu, Nat. Phys. **11**, 141 (2015).

[17] G. Wang, L. Bouet, M. Glazov, T. Amand, E. Ivchenko, E. Palleau, X. Marie, and B. Urbaszek, 2D Mater. **2**, 034002 (2015).

[18] G. Aivazian, Z. Gong, A. M. Jones, R.-L. Chu, J. Yan, D. G. Mandrus, C. Zhang, D. Cobden, W. Yao, and X. Xu, Nat. Phys. **11**, 148 (2015).

[19] R. Schmidt, A. Arora, G. Plechinger, P. Nagler, A. Granados del Águila, M. V. Ballottin, P. C. Christianen, S. Michaelis de

Vasconcellos, C. Schüller, T. Korn, and R. Bratschitsch, Phys. Rev. Lett. **117**, 077402 (2016).
[20] G. Wang, X. Marie, B. L. Liu, T. Amand, C. Robert, F. Cadiz, P. Renucci, and B. Urbaszek, Phys. Rev. Lett. **117**, 187401 (2016).
[21] Z. Sun, A. Martinez, and F. Wang, Nat. Photon. **10**, 227 (2016).
[22] C. Mai, A. Barrette, Y. Yu, Y. G. Semenov, K. W. Kim, L. Cao, and K. Gundogdu, Nano Lett. **14**, 202 (2013).
[23] J. R. Schaibley, H. Yu, G. Clark, P. Rivera, J. S. Ross, K. L. Seyler, W. Yao, and X. Xu, Nat. Rev. Mater. **1**, 16055 (2016).
[24] A. V. Stier, N. P. Wilson, K. A. Velizhanin, J. Kono, X. Xu, and S. A. Crooker, Phys. Rev. Lett. **120**, 057405 (2018).
[25] J. Zipfel, J. Holler, A. A. Mitioglu, M. V. Ballottin, P. Nagler, A. V. Stier, T. Taniguchi, K. Watanabe, S. A. Crooker, P. C. M. Christianen, T. Korn, and A. Chernikov, Phys. Rev. B **98**, 075438 (2018).
[26] E. Liu, J. van Baren, T. Taniguchi, K. Watanabe, Y.-C. Chang, and C. H. Lui, Phys. Rev. B **99**, 205420 (2019).
[27] A. V. Stier, N. P. Wilson, G. Clark, X. Xu, and S. A. Crooker, Nano Lett. **16**, 7054 (2016).
[28] A. V. Stier, K. M. McCreary, B. T. Jonker, J. Kono, and S. A. Crooker, Nat. Commun. **7**, 10643 (2016).
[29] J. Have, G. Catarina, T. G. Pedersen, and N. M. R. Peres, Phys. Rev. B **99**, 035416 (2019).
[30] T. G. Pedersen, Phys. Rev. B **94**, 125424 (2016).
[31] T. G. Pedersen, Phys. Rev. B **68**, 245104 (2003).
[32] T. Morimoto, Y. Hatsugai, and H. Aoki, Phys. Rev. Lett. **103**, 116803 (2009).
[33] J. G. Pedersen and T. G. Pedersen, Phys. Rev. B **84**, 115424 (2011).
[34] G. Catarina, J. Have, J. Fernández-Rossier, and N. M. R. Peres, Phys. Rev. B **99**, 125405 (2019).
[35] J. Have and T. G. Pedersen, Phys. Rev. B **97**, 115405 (2018).
[36] Z. Y. Zhu, Y. C. Cheng, and U. Schwingenschlögl, Phys. Rev. B **84**, 153402 (2011).
[37] T. Cheiwchanchamnangij and W. R. L. Lambrecht, Phys. Rev. B **85**, 205302 (2012).
[38] A. Kormányos, G. Burkard, M. Gmitra, J. Fabian, V. Zólyomi, N. D. Drummond, and V. Fal'ko, 2D Mater. **2**, 022001 (2015).
[39] D. Kochan, S. Irmer, and J. Fabian, Phys. Rev. B **95**, 165415 (2017).
[40] A. Taghizadeh and T. Pedersen, arXiv:1812.02596.
[41] T. G. Pedersen, Phys. Rev. B **98**, 165425 (2018).
[42] F. A. Rasmussen and K. S. Thygesen, J. Phys. Chem. C **119**, 13169 (2015).
[43] W. Kohn, Phys. Rev. **115**, 1460 (1959).
[44] J. G. Pedersen and T. G. Pedersen, Phys. Rev. B **87**, 235404 (2013).
[45] H. Rostami, R. Asgari, and F. Guinea, J. Phys.: Condens. Matter **28**, 495001 (2016).
[46] K. He, N. Kumar, L. Zhao, Z. Wang, K. F. Mak, H. Zhao, and J. Shan, Phys. Rev. Lett. **113**, 026803 (2014).
[47] M. L. Trolle, G. Seifert, and T. G. Pedersen, Phys. Rev. B **89**, 235410 (2014).
[48] L. V. Keldysh, Sov. Phys. JETP **29**, 658 (1979).
[49] M. L. Trolle, T. G. Pedersen, and V. Véniard, Sci. Rep. **7**, 39844 (2017).
[50] R. Haydock, Comput. Phys. Commun. **20**, 11 (1980).
[51] O. A. Ajayi, J. V. Ardelean, G. D. Shepard, J. Wang, A. Antony, T. Taniguchi, K. Watanabe, T. F. Heinz, S. Strauf, X. Zhu *et al.*, 2D Mater. **4**, 031011 (2017).
[52] G. Moody, C. K. Dass, K. Hao, C.-H. Chen, L.-J. Li, A. Singh, K. Tran, G. Clark, X. Xu, G. Berghäuser *et al.*, Nat. Commun. **6**, 8315 (2015).
[53] F. Cadiz, E. Courtade, C. Robert, G. Wang, Y. Shen, H. Cai, T. Taniguchi, K. Watanabe, H. Carrere, D. Lagarde *et al.*, Phys. Rev. X **7**, 021026 (2017).
[54] D. Nakamura, T. Sasaki, W. Zhou, H. Liu, H. Kataura, and S. Takeyama, Phys. Rev. B **91**, 235427 (2015).
[55] J. Qi, X. Li, Q. Niu, and J. Feng, Phys. Rev. B **92**, 121403(R) (2015).
[56] B. Scharf, G. Xu, A. Matos-Abiague, and I. Žutić, Phys. Rev. Lett. **119**, 127403 (2017).
[57] A. Ferreira, J. Viana-Gomes, Y. V. Bludov, V. Pereira, N. M. R. Peres, and A. H. Castro Neto, Phys. Rev. B **84**, 235410 (2011).
[58] H. Da, L. Gao, Y. An, H. Zhang, and X. Yan, Adv. Opt. Mater. **6**, 1701175 (2018).
[59] R. Geick, C. H. Perry, and G. Rupprecht, Phys. Rev. **146**, 543 (1966).
[60] P. Cudazzo, I. V. Tokatly, and A. Rubio, Phys. Rev. B **84**, 085406 (2011).